MOVING-WATER EQUILIBRIA PRESERVING CENTRAL-UPWIND SCHEMES FOR THE SHALLOW WATER EQUATIONS[*]

YUANZHEN CHENG[†] AND ALEXANDER KURGANOV[‡]

Abstract. We construct a new second-order moving-water equilibria preserving central-upwind scheme for the one-dimensional Saint-Venant system of shallow water equations. Special reconstruction procedure and source term discretization are the key components that guarantee the resulting scheme is capable of exactly preserving smooth moving-water steady-state solutions and a draining time-step technique ensures positivity of the water depth. Several numerical experiments are performed to verify the well-balanced and positivity preserving properties as well as the ability of the proposed scheme to accurately capture small perturbations of moving-water steady states. We also demonstrate the advantage and importance of utilizing the new method over its still-water equilibria preserving counterpart.

Key words. Shallow water equations, central-upwind scheme, well-balanced method, steady-state solutions (equilibria), moving-water and still-water equilibria.

AMS subject classifications. 76M12, 65M08, 35L65, 86-08, 86A05.

1. Introduction

The Saint-Venant system of shallow water equations plays an important role in the modeling and simulations of shallow water flows including tidal flows in estuary and coastal water regions; bore wave propagation; river, reservoir, and open channel flows, among others. In one space dimension, the Saint-Venant system reads as follows:

$$\begin{cases} h_t + q_x = 0, \\ q_t + \left(hu^2 + \dfrac{g}{2}h^2 \right)_x = -ghB_x, \end{cases} \tag{1.1}$$

where $h(x,t)$ is the water depth, $u(x,t)$ is the velocity, $q(x,t) := h(x,t)u(x,t)$ is the discharge, $B(x)$ is the bottom elevation, and g is the gravitational constant. In this paper, we will consider the variation of the bottom as the only source term, but other terms, such as friction terms, Coriolis forces, wind forces, or variations of the channel width, could also be added.

An essential feature of the shallow water equation (1.1) is that they admit steady-state solutions at which the flux gradients are exactly balanced by the source terms. The general smooth steady-state solutions of (1.1) are given by

$$q \equiv \text{Const}, \quad E := \frac{u^2}{2} + g(h+B) \equiv \text{Const}. \tag{1.2}$$

One of the most physically relevant steady state is the still-water "lake at rest" state, which represents a still flat water surface

$$q \equiv 0, \quad h + B \equiv \text{Const}. \tag{1.3}$$

Note that still-water steady state (1.3) is a special case of the general moving-water steady state (1.2) with $q \equiv 0$. Many physical phenomena correspond to small perturbations of these steady-state solutions, which are very difficult to accurately capture using

[†]Mathematics Department, Tulane University, New Orleans, LA 70118, USA (ycheng5@tulane.edu).
[‡]Mathematics Department, Tulane University, New Orleans, LA 70118, USA (kurganov@math.tulane.edu).

a coarse grid unless the numerical scheme exactly preserves the unperturbed steady state at the discrete level. If the scheme preserves the steady state up to the order of its formal accuracy, the spurious numerical waves may have larger magnitude than the water waves to be captured. This difficulty can be cured by using a very fine mesh, which in practice can be unaffordable. It is, therefore, necessary to design the schemes capable of exactly preserving still-water steady-state solution (1.3). In the literature (see, e.g., [1, 2, 3, 5, 7, 12, 14, 17, 20, 24, 25]), such schemes are usually called well-balanced.

It is, however, significantly more difficult to obtain well-balanced schemes capable of exactly preserving moving-water steady states. This goal has been achieved, for example, in the following papers: a class of first-order accurate flux-vector-splitting schemes based on the theory of nonconservative products was proposed in [8]; well-balanced second-order central schemes on staggered grids were introduced in [26]; numerical methods based on local subsonic steady state reconstruction, which are exactly well-balanced for subsonic moving equilibria, was presented in [4]; high-order weighted essentially nonoscillatory (WENO) methods were designed in [23, 35, 34]; central WENO methods were proposed in [27]; path-conservative WENO methods were introduced in [6]; and high-order discontinuous Galerkin (DG) methods were presented in [33, 34].

Another numerical challenge is related to the computation of solutions when the water depth h is very small or even zero. In this regime, even small numerical oscillations in the computed solutions may lead to appearance of negative computed h, which is not only physically irrelevant, but also causes the numerical scheme to break down since the eigenvalues of the system (1.1) are $u \pm \sqrt{gh}$. There are many numerical methods in the literature (see, e.g., [1, 2, 3, 17, 24]), which are both well-balanced in the sense of exactly preserving still-water steady states and positivity preserving of h. However, to the best of our knowledge, the DG method developed in [33] is the only one capable of both exactly preserving moving-water steady states and positivity of h.

In this paper, we develop a central-upwind scheme that can exactly preserve moving-water equilibria and positivity of the water depth. Central-upwind schemes were proposed in [19, 16, 15] in the context of general multidimensional systems of conservation laws. They were extended to shallow water equations in [14, 17], where well-balanced central-upwind schemes capable of exactly preserving still-water equilibria were introduced.

The first key component in designing well-balanced central-upwind schemes is the use of piecewise polynomial reconstructions of equilibrium variables q and E rather than conservative ones (h and q). In [14, 17], a water surface variable $w := h + B$ was used instead of h. To preserve the moving-water steady state, we reconstruct the equilibrium variable $E = \frac{1}{2}u^2 + g(h + B)$ (the details on the proposed well-balanced reconstruction can be found in Section 3.1). The second key component in the construction of the proposed well-balanced central-upwind scheme is a special discretization of the source term (see Section 3.2). Finally, the positivity of the computed water depth is ensured by using the draining time-step technique from [2, 3].

The paper is organized as follows. In Section 2, we give a brief review of the central-upwind scheme for the one-dimensional shallow water equations. The moving-water equilibria preserving central-upwind scheme is presented in Section 3. Finally, Section 4 contains several numerical examples. We demonstrate that smooth moving-water equilibria are preserved up to machine accuracy and small perturbations of such equilibria are sharply resolved. We also provide carefully selected examples to show the advantage of the well-balanced schemes preserving moving-water equilibria over their counterparts capable of preserving still-water equilibria only.

2. Central-upwind scheme — a brief overview

In this section, we give a short overview of the second-order semi-discrete central-upwind scheme for the hyperbolic system of balance laws

$$\boldsymbol{U}_t + \boldsymbol{F}(\boldsymbol{U})_x = \boldsymbol{S}(\boldsymbol{U}). \tag{2.1}$$

For more details, we refer to [15, 16, 19, 14, 17, 18].

For simplicity, we introduce a uniform spatial grid $x_\alpha := \alpha \Delta x$, where Δx is a small spatial scale and α is any spatial index, either integer or half-integer. We denote by I_j the finite volume cells $I_j := [x_{j-\frac{1}{2}}, x_{j+\frac{1}{2}}]$ and by $\overline{\boldsymbol{U}}_j$ and $\overline{\boldsymbol{S}}_j$ the cell averages

$$\overline{\boldsymbol{U}}_j \approx \frac{1}{\Delta x} \int_{I_j} \boldsymbol{U}(x)\,dx \quad \text{and} \quad \overline{\boldsymbol{S}}_j \approx \frac{1}{\Delta x} \int_{I_j} \boldsymbol{S}(\boldsymbol{U}(x))\,dx$$

of the computed solution $\boldsymbol{U}$ and source term $\boldsymbol{S}$, respectively. A central-upwind semi-discretization of (2.1) is the following system of ODEs:

$$\frac{d}{dt}\overline{\boldsymbol{U}}_j = -\frac{\boldsymbol{H}_{j+\frac{1}{2}} - \boldsymbol{H}_{j-\frac{1}{2}}}{\Delta x} + \overline{\boldsymbol{S}}_j, \tag{2.2}$$

which should be numerically integrated by an appropriate (stable, sufficiently accurate and efficient) ODE solver. The central-upwind numerical flux $\boldsymbol{H}_{j+\frac{1}{2}}$ from [16] is

$$\boldsymbol{H}_{j+\frac{1}{2}} := \frac{a_{j+\frac{1}{2}}^+ \boldsymbol{F}(\boldsymbol{U}_{j+\frac{1}{2}}^-) - a_{j+\frac{1}{2}}^- \boldsymbol{F}(\boldsymbol{U}_{j+\frac{1}{2}}^+)}{a_{j+\frac{1}{2}}^+ - a_{j+\frac{1}{2}}^-} + \frac{a_{j+\frac{1}{2}}^+ a_{j+\frac{1}{2}}^-}{a_{j+\frac{1}{2}}^+ - a_{j+\frac{1}{2}}^-}\left[\boldsymbol{U}_{j+\frac{1}{2}}^+ - \boldsymbol{U}_{j+\frac{1}{2}}^-\right]. \tag{2.3}$$

Here, $\boldsymbol{U}_{j+\frac{1}{2}}^\pm$ are the right/left point values of the piecewise linear reconstruction

$$\widetilde{\boldsymbol{U}}(x) = \overline{\boldsymbol{U}}_j + (\boldsymbol{U}_x)_j (x - x_j), \quad x \in I_j, \tag{2.4}$$

at $x = x_{j+\frac{1}{2}}$, namely,

$$\boldsymbol{U}_{j+\frac{1}{2}}^+ = \overline{\boldsymbol{U}}_{j+1} - \frac{\Delta x}{2}(\boldsymbol{U}_x)_{j+1}, \quad \boldsymbol{U}_{j+\frac{1}{2}}^- = \overline{\boldsymbol{U}}_j + \frac{\Delta x}{2}(\boldsymbol{U}_x)_j. \tag{2.5}$$

The numerical derivatives $(\boldsymbol{U}_x)_j$ are (at least) first-order, component-wise approximations of $\boldsymbol{U}_x(x_j, t)$, computed using a nonlinear limiter needed to ensure a non-oscillatory nature of the reconstruction (2.4). In our numerical experiments, we have used the generalized minmod limiter (see, e.g., [21, 22, 30, 31])

$$(\boldsymbol{U}_x)_j = \operatorname{minmod}\left(\theta \frac{\overline{\boldsymbol{U}}_j - \overline{\boldsymbol{U}}_{j-1}}{\Delta x}, \frac{\overline{\boldsymbol{U}}_{j+1} - \overline{\boldsymbol{U}}_{j-1}}{2\Delta x}, \theta \frac{\overline{\boldsymbol{U}}_{j+1} - \overline{\boldsymbol{U}}_j}{\Delta x}\right), \quad \theta \in [1,2]. \tag{2.6}$$

The minmod function is defined as

$$\operatorname{minmod}(z_1, z_2, \ldots) := \begin{cases} \min_j\{z_j\}, & \text{if } z_j > 0, \forall j, \\ \max_j\{z_j\}, & \text{if } z_j < 0, \forall j, \\ 0, & \text{otherwise,} \end{cases}$$

and the parameter θ can be used to control the amount of numerical viscosity present in the resulting scheme. We recall that larger values of θ correspond to less dissipative

but, in general, more oscillatory reconstructions, see [21, 22]. The right- and left-sided local speeds $a_{j+\frac{1}{2}}^{\pm}$ in (2.3) are obtained from the largest and smallest eigenvalues of the Jacobian matrix $A := \partial \boldsymbol{F}/\partial \boldsymbol{U}$. In the case of convex fluxes, the local speeds can be estimated as follows:

$$a_{j+\frac{1}{2}}^{+} := \max\left\{ \lambda_N\left(A(\boldsymbol{U}_{j+\frac{1}{2}}^{-})\right), \lambda_N\left(A(\boldsymbol{U}_{j+\frac{1}{2}}^{+})\right), 0 \right\},$$
$$a_{j+\frac{1}{2}}^{-} := \min\left\{ \lambda_1\left(A(\boldsymbol{U}_{j+\frac{1}{2}}^{-})\right), \lambda_1\left(A(\boldsymbol{U}_{j+\frac{1}{2}}^{+})\right), 0 \right\}.$$

The construction of the scheme will be completed once one specifies a quadrature for $\overline{\boldsymbol{S}}_j$. Note that the quantities $\overline{\boldsymbol{U}}_j$, $\boldsymbol{U}_{j+\frac{1}{2}}^{\pm}$, $(\boldsymbol{U}_x)_j$, $\overline{\boldsymbol{S}}_j$, and $\boldsymbol{H}_{j+\frac{1}{2}}$ depend on t, but we suppress this dependence throughout the paper for brevity.

2.1. Still-water equilibria preserving central-upwind scheme. In this section, we briefly overview the well-balanced semi-discrete central-upwind scheme for the Saint-Venant system (1.1). We describe the scheme from [17], which is capable of exactly preserving still-water equilibria only. Following [14, 17], we rewrite the system (1.1) in an equivalent form in terms of the equilibrium variables $w := h + B$ and q rather than the conservative ones (h and q)

$$\begin{cases} w_t + q_x = 0, \\ q_t + \left(\dfrac{q^2}{w-B} + \dfrac{g}{2}(w-B)^2 \right)_x = -g(w-B)B_x. \end{cases} \tag{2.7}$$

This system can be recast in the vector form (2.1) with

$$\boldsymbol{U} = (w,q)^T, \quad \boldsymbol{F}(\boldsymbol{U},B) = \left(q, \frac{q^2}{w-B} + \frac{g}{2}(w-B)^2 \right)^T, \quad \boldsymbol{S}(\boldsymbol{U},B) = (0, -g(w-B)B_x)^T.$$

The central-upwind scheme described above directly applies to the system (2.7).

As it has been shown in [17], the central-upwind scheme will be well-balanced provided the source term is discretized using the following "well-balanced" quadrature:

$$\overline{\boldsymbol{S}}_j^{(2)} = -g \frac{w_{j+\frac{1}{2}}^{-} - B_{j+\frac{1}{2}} + w_{j-\frac{1}{2}}^{+} - B_{j-\frac{1}{2}}}{2} \cdot \frac{B_{j+\frac{1}{2}} - B_{j-\frac{1}{2}}}{\Delta x},$$

where $B_{j+\frac{1}{2}} := \frac{1}{2}\left(B(x_{j+\frac{1}{2}} + 0) + B(x_{j+\frac{1}{2}} - 0) \right)$, which reduces to $B_{j+\frac{1}{2}} := B(x_{j+\frac{1}{2}})$ in the case of smooth B.

3. Moving-water equilibria preserving central-upwind scheme

In this section, we propose a new well-balanced central-upwind scheme, which is capable of exactly preserving not only "lake at rest" states, but the entire family of smooth steady-state solutions (1.2). First of all, we do not rewrite the Saint-Venant system, but apply the central-upwind scheme directly to its original formulation (1.1), which can be written in the vector form (2.1) with

$$\boldsymbol{U} = (h,q)^T, \quad \boldsymbol{F}(\boldsymbol{U}) = \left(q, \frac{q^2}{h} + \frac{g}{2}h^2 \right)^T, \quad \boldsymbol{S}(\boldsymbol{U},B) = (0, -ghB_x)^T.$$

However, a direct application of the scheme described in Section 2 will not result in a well-balanced, positivity preserving method. We therefore need to make the following three modifications.

3.1. Variable transformation. One main component of the new well-balanced central-upwind scheme is reconstruction of the equilibrium variables, which are now q and E. To this end, we first compute the values of E at the cell centers

$$E_j = \frac{\bar{q}_j^2}{2\bar{h}_j^2} + g(\bar{h}_j + B_j),$$

where $B_j := (B_{j+\frac{1}{2}} + B_{j-\frac{1}{2}})/2$. Secondly, we compute the point values $q_{j+\frac{1}{2}}^{\pm}$ using the reconstruction (2.4)–(2.6) and the point values $E_{j+\frac{1}{2}}^{\pm}$ are obtained similarly:

$$E_{j+\frac{1}{2}}^+ = E_{j+1} - \frac{\Delta x}{2}(E_x)_{j+1}, \quad E_{j+\frac{1}{2}}^- = E_j + \frac{\Delta x}{2}(E_x)_j,$$

with

$$(E_x)_j = \operatorname{minmod}\left(\theta\frac{E_j - E_{j-1}}{\Delta x}, \frac{E_{j+1} - E_{j-1}}{2\Delta x}, \theta\frac{E_{j+1} - E_j}{\Delta x}\right), \quad \theta \in [1,2].$$

Finally, equipped with $q_{j+\frac{1}{2}}^{\pm}$ and $E_{j+\frac{1}{2}}^{\pm}$, we need to recover the corresponding point values $h_{j+\frac{1}{2}}^{\pm}$. This is done using the technique presented in [23]. Given q, E, and B, we look for a solution of the following nonlinear algebraic equation:

$$\varphi(h) := \frac{q^2}{2h^2} + g(h+B) - E = 0. \tag{3.1}$$

In fact, the solution of this equation may not be unique. To single out the physically relevant solution, we proceed as follows. If $q=0$, the variable transformation is trivial: $h = E/g - B$. If $q \neq 0$, then the function $\varphi(h)$ is convex and attains its minimum value at

$$h_0 = \left(\frac{q^2}{g}\right)^{\frac{1}{3}}.$$

Note that h_0 corresponds to the sonic point (that is, the Froude number $Fr := |u|/\sqrt{gh} = 1$ at $h = h_0$). When $h < h_0$ ($h > h_0$), we have $Fr > 1$ ($Fr < 1$) and a state is called supersonic (subsonic).

If $Fr = 1$, then the unique solution of (3.1) is $h = h_0$. Otherwise, equation (3.1) has to be solved using a numerical method. We use Newton's method, which is known to be only locally convergent and thus requires a good initial guess h_*. If $Fr > 1$, then we need $h_* < h_0$ while if $Fr < 1$, the requirement on h_* is opposite: $h_* > h_0$. In both cases, monotone quadratic convergence of Newton's method will be guaranteed if we impose an additional restriction on h_*: $\varphi(h_*) > 0$.

When equation (3.1) is solved at the cell interface $x = x_{j+\frac{1}{2}}$, we will need to find two values of h, $h_{j+\frac{1}{2}}^+$, and $h_{j+\frac{1}{2}}^-$, by solving

$$\frac{(q_{j+\frac{1}{2}}^+)^2}{2(h_{j+\frac{1}{2}}^+)^2} + g(h_{j+\frac{1}{2}}^+ + B_{j+\frac{1}{2}}) - E_{j+\frac{1}{2}}^+ = 0 \tag{3.2}$$

and

$$\frac{(q_{j+\frac{1}{2}}^-)^2}{2(h_{j+\frac{1}{2}}^-)^2} + g(h_{j+\frac{1}{2}}^- + B_{j+\frac{1}{2}}) - E_{j+\frac{1}{2}}^- = 0, \tag{3.3}$$

respectively. The choice of an initial guess for these equations is based on the values of the corresponding Froude numbers

$$Fr^+_{j+\frac{1}{2}} := \frac{|\bar{q}_{j+1}|}{\sqrt{g\bar{h}^3_{j+1}}} \quad and \quad Fr^-_{j+\frac{1}{2}} := \frac{|\bar{q}_j|}{\sqrt{g\bar{h}^3_j}}.$$

To find a proper h_*, we use the following approach. Consider, for example, equation (3.2). If $Fr^+_{j+\frac{1}{2}} > 1$, we then select h_* according to the following algorithm.

ALGORITHM 3.1 (initial guess selection in the supersonic case).

    Step 1: Set $h_* := \min(h_0, \bar{h}_{j+1})$ and $h_0 = \sqrt[3]{(q^+_{j+\frac{1}{2}})^2/g}$;

    Step 2: Compute $\varphi(h_*)$;

    Step 3: If $\varphi(h_*) < \varepsilon$, set $h_* := \lambda_1 h_*$ and go back to Step 2.

If $Fr^+_{j+\frac{1}{2}} < 1$, then h_* is selected as follows:

ALGORITHM 3.2 (initial guess selection in the subsonic case).

    Step 1: Set $h_* := \max(h_0, \bar{h}_{j+1})$ and $h_0 = \sqrt[3]{(q^+_{j+\frac{1}{2}})^2/g}$;

    Step 2: Compute $\varphi(h_*)$;

    Step 3: If $\varphi(h_*) < \varepsilon$, set $h_* := \lambda_2 h_*$ and go back to Step 2.

In all of our numerical experiments, we have used $\varepsilon = 10^{-4}, \lambda_1 = 0.9, \lambda_2 = 1.1$. For equation (3.3), the value of h_* is selected similarly (the only difference is that in Step 1, $\bar{h}_{j+1}$ and $q^+_{j+\frac{1}{2}}$ are replaced with $\bar{h}_j$ and $q^-_{j+\frac{1}{2}}$, respectively). In the neighborhood ef the sonic point, Newton's method might diverge, and in this case, we set $h = h_0$.

REMARK 3.1.   We note that in the cells where $\bar{h}_j$ is small, our numerical experiments clearly demonstrate that the variable transformation described in this section may become unstable. Therefore, in the cells with $\bar{h}_j < 10^{-8}$, we use the first-order piecewise constant reconstruction, namely, we set

$$h^+_{j-\frac{1}{2}} = h^-_{j+\frac{1}{2}} = \bar{h}_j \quad and \quad q^+_{j-\frac{1}{2}} = q^-_{j+\frac{1}{2}} = \bar{q}_j.$$

3.2. Well-balanced discretization of the source term.   In this section, we describe the second major component of the new well-balanced central-upwind scheme – a well-balanced discretization of $\overline{S}_j$ such that the general moving-water steady-state solution (1.2) will be preserved by the scheme (2.2),(2.3). To this end, we substitute the steady-state data $q(x) \equiv \widehat{q}, E(x) \equiv \widehat{E}$ into the semi-discrete scheme and compute the numerical fluxes. The first component of the flux is

$$H^{(1)}_{j+\frac{1}{2}} = \widehat{q} + \frac{a^+_{j+\frac{1}{2}} a^-_{j+\frac{1}{2}}}{a^+_{j+\frac{1}{2}} - a^-_{j+\frac{1}{2}}} (h^+_{j+\frac{1}{2}} - h^-_{j+\frac{1}{2}}).$$

Since we reconstruct the equilibrium variables q and E, we obtain $q^+_{j+\frac{1}{2}} \equiv q^-_{j+\frac{1}{2}} \equiv \widehat{q}$ and $E^+_{j+\frac{1}{2}} \equiv E^-_{j+\frac{1}{2}} \equiv \widehat{E}$ and hence $h^+_{j+\frac{1}{2}} = h^-_{j+\frac{1}{2}} =: h_{j+\frac{1}{2}}$ for all j. Therefore,

$$\frac{H^{(1)}_{j+\frac{1}{2}} - H^{(1)}_{j-\frac{1}{2}}}{\Delta x} = \frac{\widehat{q} - \widehat{q}}{\Delta x} = 0.$$

The second component of the flux is reduced to

$$H^{(2)}_{j+\frac{1}{2}} = \frac{\widehat{q}^2}{h_{j+\frac{1}{2}}} + \frac{g}{2}h^2_{j+\frac{1}{2}},$$

and then

$$H^{(2)}_{j+\frac{1}{2}} - H^{(2)}_{j-\frac{1}{2}} = \widehat{q}^2\left(\frac{1}{h_{j+\frac{1}{2}}} - \frac{1}{h_{j-\frac{1}{2}}}\right) + \frac{g}{2}(h_{j+\frac{1}{2}} - h_{j-\frac{1}{2}})(h_{j+\frac{1}{2}} + h_{j-\frac{1}{2}}). \qquad (3.4)$$

Since $E_{j+\frac{1}{2}} = E_{j-\frac{1}{2}}$, we have

$$g(h_{j+\frac{1}{2}} - h_{j-\frac{1}{2}}) = \frac{\widehat{q}^2}{2}\left(\frac{1}{h^2_{j+\frac{1}{2}}} - \frac{1}{h^2_{j-\frac{1}{2}}}\right) - g(B_{j+\frac{1}{2}} - B_{j-\frac{1}{2}}), \qquad (3.5)$$

and substituting (3.5) into (3.4) results in

$$\frac{H^{(2)}_{j+\frac{1}{2}} - H^{(2)}_{j-\frac{1}{2}}}{\Delta x} = -g\frac{h_{j+\frac{1}{2}} + h_{j-\frac{1}{2}}}{2} \cdot \frac{B_{j+\frac{1}{2}} - B_{j-\frac{1}{2}}}{\Delta x} + \frac{h_{j+\frac{1}{2}} - h_{j-\frac{1}{2}}}{4\Delta x}\left(\frac{\widehat{q}}{h_{j+\frac{1}{2}}} - \frac{\widehat{q}}{h_{j-\frac{1}{2}}}\right)^2. \qquad (3.6)$$

Therefore, in order to preserve the moving-water steady state, the contribution of fluxes, (3.6), must be the same as the contribution of the source term. This dictates the following discretization of the cell average of the source term

$$\overline{S}^{(2)}_j = -g\frac{h^-_{j+\frac{1}{2}} + h^+_{j-\frac{1}{2}}}{2} \cdot \frac{B_{j+\frac{1}{2}} - B_{j-\frac{1}{2}}}{\Delta x} + \frac{h^-_{j+\frac{1}{2}} - h^+_{j-\frac{1}{2}}}{4\Delta x}(u^-_{j+\frac{1}{2}} - u^+_{j-\frac{1}{2}})^2, \qquad (3.7)$$

where $u^\pm_{j+\frac{1}{2}} := q^\pm_{j+\frac{1}{2}}/h^\pm_{j+\frac{1}{2}}$. Notice that the obtained quadrature (3.7) is second-order accurate since the term $(u^-_{j+\frac{1}{2}} - u^+_{j-\frac{1}{2}})^2 = \mathcal{O}((\Delta x)^2)$ for smooth solutions.

REMARK 3.2. The quadrature (3.7) was derived in [23] in the context of WENO schemes, for which the order of the quadrature was increased using a Richardson extrapolation technique.

3.3. Positivity preserving via draining time step technique. In this section, we describe the technique originally proposed in [3], which we use to guarantee positivity of the computed water depth: The outgoing fluxes in draining cells are limited according to the following algorithm, which we present in the case of forward Euler time discretization of (2.2):

$$\overline{h}^{n+1}_j = \overline{h}^n_j - \frac{\Delta t}{\Delta x}\left(H^{(1)}_{j+\frac{1}{2}} - H^{(1)}_{j-\frac{1}{2}}\right). \qquad (3.8)$$

Here, the numerical fluxes are evaluated at time level $t = t^n$ and Δt is the time step restricted by (see [17])

$$\frac{\Delta t}{\Delta x}\max_j|a^\pm_{j+\frac{1}{2}}| \leq \frac{1}{2}. \qquad (3.9)$$

To guarantee the positivity of $\overline{h}^{n+1}_j$ provided $\overline{h}^n_j \geq 0, \forall j$, we first introduce the so-called draining time step

$$\Delta t^{drain}_j := \frac{\Delta x\overline{h}^n_j}{\max\left(0, H^{(1)}_{j+\frac{1}{2}}\right) + \max\left(0, -H^{(1)}_{j-\frac{1}{2}}\right)},$$

which describes the time when the water contained in cell j in the beginning of the time step have left via the outflow fluxes. We then replace the evolution step (3.8) by

$$\bar{h}_j^{n+1} = \bar{h}_j^n - \frac{\Delta t_{j+\frac{1}{2}} H_{j+\frac{1}{2}}^{(1)} - \Delta t_{j-\frac{1}{2}} H_{j-\frac{1}{2}}^{(1)}}{\Delta x}, \tag{3.10}$$

where we set the effective time steps at the cell interfaces to be

$$\Delta t_{j+\frac{1}{2}} = \min\left(\Delta t, \Delta t_i^{drain}\right), \quad i = j + \frac{1}{2} - \frac{\operatorname{sgn}\left(H_{j+\frac{1}{2}}^{(1)}\right)}{2},$$

with Δt satisfying (3.9). Thus, we have $\bar{h}_j^{n+1} \geq 0, \forall j$.

A higher-order time discretization can be obtained using strong stability preserving (SSP) ODE solvers, which can be represented as convex combinations of forward Euler time steps (see, e.g., [9, 10, 28, 29]). Positivity preserving SSP methods are thus obtained by replacing the forward Euler steps (3.8) by the modified ones (3.10).

REMARK 3.3.   We note that in (almost) dry regions, the computed values of h can be very small or even zero. This may not allow one to (accurately) compute the values of the velocity u, which may become artificially large. We therefore desingularize the velocity computation as follows:

$$u_{j+\frac{1}{2}}^{\pm} = \begin{cases} \dfrac{q_{j+\frac{1}{2}}^{\pm}}{h_{j+\frac{1}{2}}^{\pm}}, & \text{if } h_{j+\frac{1}{2}}^{\pm} > \varepsilon, \\[4mm] 0, & \text{otherwise.} \end{cases}$$

For consistency, $q_{j+\frac{1}{2}}^{\pm}$ are then recomputed using $q_{j+\frac{1}{2}}^{\pm} = h_{j+\frac{1}{2}}^{\pm} \cdot u_{j+\frac{1}{2}}^{\pm}$. In all of our numerical experiments, we have taken $\varepsilon = 10^{-8}$. One may use other desingularization strategies (see, e.g., the discussion in [17]).

4. Numerical examples

In this section, we demonstrate the performance of the proposed moving-water equilibria preserving central-upwind scheme (New Scheme) and compare it with its still-water equilibria preserving counterpart (Old Scheme) from [17]. In all of the examples, we integrate the ODE system (2.2) using the third-order SSP Runge–Kutta ODE solver (see, e.g., [9, 10, 28, 29]). We also set:

• the gravitational constant $g = 9.812$;

• the computational domain $[0, 25]$ (except for Example 1);

• the minmod parameter $\theta = 1.3$;

• the CFL number 0.5.

Example 1 — accuracy test. In this example, taken from [23, 17], we check the experimental rate of convergence. The initial data and the bottom topography function are

$$h(x,0) = 5 + e^{\cos(2\pi x)}, \quad q(x,0) = \sin(\cos(2\pi x)), \quad B(x) = \sin^2(\pi x),$$

and the 1-periodic boundary conditions are imposed.

Though the exact solution is not known explicitly for this initial-boundary value problem, it seems to be a generic problem for accuracy tests since most known solutions

(in closed form) have special properties making the leading term in truncation errors in many schemes vanish. We use the New Scheme with 51200 uniform cells to compute a reference solution, and then use it to compute numerical errors. The solution at time $t=0.1$ is still smooth (shocks develop later in time for this problem) and we thus compute it and measure the L^1-errors for both h and q. The results are reported on Table 4.1, where one can clearly observe the experimental second order of accuracy.

Number of	h		q	
grid cells	L^1-error	Rate	L^1-error	Rate
100	3.82×10^{-3}	–	3.53×10^{-2}	–
200	1.04×10^{-3}	1.88	8.39×10^{-3}	2.07
400	2.62×10^{-4}	1.99	2.05×10^{-3}	2.03
800	6.45×10^{-5}	2.02	5.03×10^{-4}	2.03
1600	1.60×10^{-5}	2.01	1.25×10^{-4}	2.01
3200	3.98×10^{-6}	2.01	3.10×10^{-5}	2.01

TABLE 4.1. *Example 1: L^1-errors and experimental convergence rates.*

Example 2 — well-balanced test. In this example, we verify the well-balanced property of the New Scheme. We consider both the continuous,

$$B(x) = \begin{cases} 0.2 - 0.05(x-10)^2, \text{ if } 8 \le x \le 12, \\ 0, \qquad\qquad\qquad\quad \text{otherwise,} \end{cases} \tag{4.1}$$

and discontinuous,

$$B(x) = \begin{cases} 0.2, \text{ if } 8 \le x \le 12, \\ 0, \quad \text{otherwise,} \end{cases} \tag{4.2}$$

bottom topography functions and the following three sets of initial data:

(a) *Supercritical (supersonic) flow* with

$$q(x,0) \equiv 24, \quad E(x,0) \equiv \frac{24^2}{2 \times 2^2} + 9.812 \times 2; \tag{4.3}$$

(b) *Subcritical (subsonic) flow* with

$$q(x,0) \equiv 4.42, \quad E(x,0) \equiv \frac{4.42^2}{2 \times 2^2} + 9.812 \times 2; \tag{4.4}$$

(c) *Transcritical (transonic) flow* with

$$q(x,0) \equiv 1.53, \quad E(x,0) \equiv \frac{3}{2}(9.812 \times 1.53)^{\frac{2}{3}} + 9.812 \times 0.2. \tag{4.5}$$

We thus consider altogether six different initial value problems (IVP); cases (b) and (c) with B given by (4.1) are taken from [23].

We compute the solutions of these IVPs until the final time $t=20$ using 200 uniform cells and observe that all of the steady-state solutions (4.3)–(4.5) are preserved within

the machine accuracy. This verifies the desired well-balanced property of the New Scheme.

REMARK 4.1.   In this example, the initial data are given in terms of $\{\bar{q}_j(0)\}$ and $\{\bar{E}_j(0)\}$. To obtain $\bar{h}_j(0)$, we solve the nonlinear algebraic equation (3.1) using Newton's method; see Section 3.1. To this end, we need to determine whether the Froude number is smaller or greater than 1 and also to choose a proper value of h_* in every cell j. In the supercritical case (a), the Froude number is larger than 1 throughout the computational domain. Similarly, in the subcritical case (b), the Froude number is smaller than 1 everywhere. In the transcritical case (c), the value of $Fr_j(0)$ depends on the shape of the bottom topography function: if B is given by (4.1), then

$$\begin{cases} Fr_j(0) < 1, \text{ if } x_j < 10, \\ Fr_j(0) > 1, \text{ if } x_j > 10, \end{cases}$$

and if B is given by (4.2), then

$$\begin{cases} Fr_j(0) < 1, \text{ if } x_j < 8, \\ Fr_j(0) = 1, \text{ if } 8 \leq x_j \leq 12, \\ Fr_j(0) > 1, \text{ if } x_j > 12. \end{cases}$$

Finally, in every cell j we choose $h_* := h_0 = \sqrt[3]{\bar{q}_j^2/g}$.

Example 3 — convergence to steady states (continuous bottom topography). In this example, we study the convergence in time towards steady flow over a bump. The bottom topography function is continuous and given by (4.1). Depending on the initial and boundary conditions, the flow may be subcritical, supercritical, transcritical with or without a steady shock. We consider the following four sets of initial and boundary data (cases (b)–(d) are taken from [11, 32]; case (a) is similar to a test problem considered in [13]):

(a) *Supercritical flow* with

$$\begin{aligned} h(x,0) &= 2 - B(x), \quad q(x,0) \equiv 0, \\ h(0,t) &= 2, \quad q(0,t) = 24; \end{aligned}$$

(b) *Subcritical flow* with

$$\begin{aligned} h(x,0) &= 2 - B(x), \quad q(x,0) \equiv 0, \\ q(0,t) &= 4.42, \quad h(25,t) = 2; \end{aligned}$$

(c) *Transcritical flow without a shock* with

$$\begin{aligned} h(x,0) &= 0.66 - B(x), \quad q(x,0) \equiv 0, \\ q(0,t) &= 1.53, \quad h(25,t) = 0.66. \end{aligned}$$

(d) *Transcritical flow with a shock* with

$$\begin{aligned} h(x,0) &= 0.33 - B(x), \quad q(x,0) \equiv 0, \\ q(0,t) &= 0.18, \quad h(25,t) = 0.33. \end{aligned}$$

REMARK 4.2. In case (c), the downstream boundary condition $(h(25,t)=0.66)$ is imposed only when the flow is subsonic.

For all these four cases, we compare the numerical solutions obtained by the New and Old Schemes at $t=200$ using 200 uniform cells. Numerical results are shown in figures 4.1–4.4. As one can see, h obtained by the New and Old Schemes are very close to the corresponding steady states in all four cases. On the other hand, in cases (a)–(c), only the New Scheme accurately captures both q and E. In case (d), the error in q and E at the shock is $\mathcal{O}(1)$ for both the New and Old Schemes. This result is expected since neither of the studied schemes preserves nonsmooth steady states.
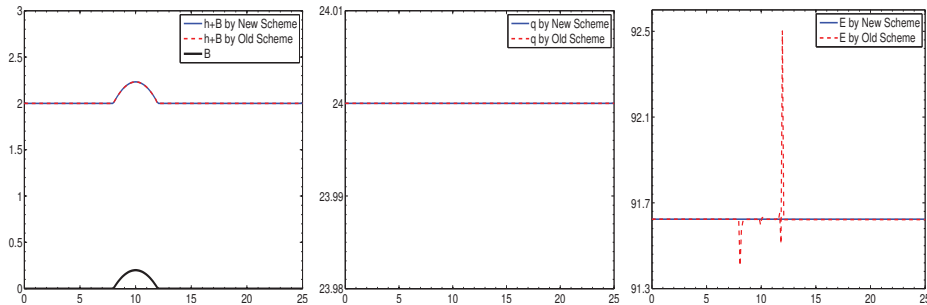
FIG. 4.1. *Example 3, case (a): $h+B$ (left), q (middle), and E (right) computed by the New and Old Schemes.*
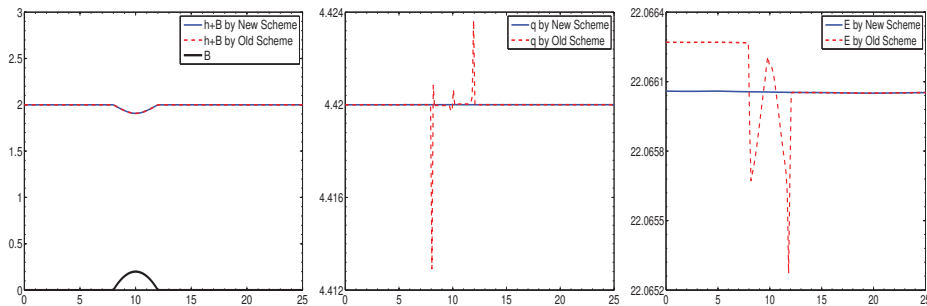
FIG. 4.2. *Example 3, case (b): $h+B$ (left), q (middle), and E (right) computed by the New and Old Schemes.*

Finally, we study the efficiency of the New and Old Schemes by running the simulation until large times when the steady state has been already reached (the final times are 200 in cases (a) and (c) and 500 in case (b)). We measure the CPU times vs. the L^1-norm of the h-, q-, and E-errors. The obtained results are reported in tables 4.2–4.4. As one can see, the New Scheme uses about 3–4 times larger CPU times, but it achieves much higher accuracy in all of the studied cases.

Example 4 — small perturbations of moving-water equilibria (continuous bottom topography). In this example, we test the ability of the New and Old Schemes to capture small perturbations of the moving-water equilibria studied in Example 2 with the continuous bottom topography function (4.1). The perturbations are
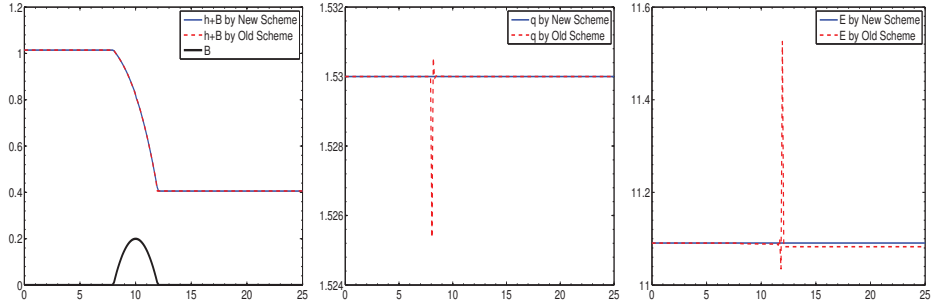
FIG. 4.3. *Example 3, case (c):* $h+B$ *(left),* q *(middle), and* E *(right) computed by the New and Old Schemes.*
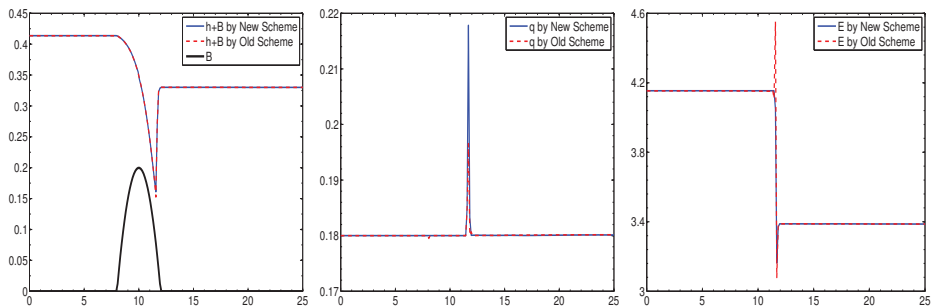
FIG. 4.4. *Example 3, case (d):* $h+B$ *(left),* q *(middle), and* E *(right) computed by the New and Old Schemes.*

Scheme	Final time	CPU time	h-error	q-error	E-error
Old	200	8.5645	3.19×10^{-3}	1.19×10^{-11}	1.98×10^{-1}
	300	12.808	3.19×10^{-3}	1.19×10^{-11}	1.98×10^{-1}
	400	16.162	3.19×10^{-3}	1.19×10^{-11}	1.98×10^{-1}
	500	20.935	3.19×10^{-3}	1.19×10^{-11}	1.98×10^{-1}
New	200	28.517	2.49×10^{-12}	1.39×10^{-11}	7.11×10^{-11}
	300	41.855	2.49×10^{-12}	1.39×10^{-11}	7.11×10^{-11}
	400	56.894	2.49×10^{-12}	1.39×10^{-11}	7.11×10^{-11}
	500	70.466	2.49×10^{-12}	1.39×10^{-11}	7.11×10^{-11}

TABLE 4.2. *Example 3, case (a): CPU times vs.* L^1*-errors.*

obtained by adding a small positive number η to the water depth for $x \in [5.75, 6.25]$ in cases (a)–(c) given by (4.3)–(4.5), respectively. We note that the same perturbations of the steady-state solutions (4.4) and (4.5) were considered in [35].

We first take $\eta = 0.05$ and compute the numerical solutions using the New and Old Schemes until $t = 1$ in case (a) and $t = 1.5$ in cases (b) and (c) with 100 uniform cells. In figures 4.5–4.7, we compare the difference between the obtained h and the background

Scheme	Final time	CPU time	h-error	q-error	E-error
Old	200	3.4476	6.16×10^{-4}	1.79×10^{-3}	2.56×10^{-3}
	300	5.1636	6.06×10^{-4}	1.74×10^{-3}	2.48×10^{-3}
	400	6.9576	6.06×10^{-4}	1.74×10^{-3}	2.48×10^{-3}
	500	8.7517	6.06×10^{-4}	1.74×10^{-3}	2.48×10^{-3}
New	200	11.965	1.11×10^{-5}	5.27×10^{-5}	1.07×10^{-4}
	300	17.846	1.40×10^{-8}	2.68×10^{-8}	8.17×10^{-8}
	400	23.806	9.32×10^{-12}	5.17×10^{-11}	1.25×10^{-10}
	500	29.952	1.08×10^{-13}	2.61×10^{-12}	3.65×10^{-12}

TABLE 4.3. *Example 3, case (b): CPU times vs. L^1-errors.*

Scheme	Final time	CPU time	h-error	q-error	E-error
Old	200	3.1980	9.33×10^{-3}	6.61×10^{-4}	1.75×10^{-1}
	300	4.8516	9.33×10^{-3}	6.61×10^{-4}	1.75×10^{-1}
	400	6.0840	9.33×10^{-3}	6.61×10^{-4}	1.75×10^{-1}
	500	7.3164	9.33×10^{-3}	6.61×10^{-4}	1.75×10^{-1}
New	200	9.8905	9.20×10^{-13}	2.30×10^{-12}	9.84×10^{-12}
	300	14.836	9.20×10^{-13}	2.30×10^{-12}	9.84×10^{-12}
	400	19.859	9.20×10^{-13}	2.30×10^{-12}	9.84×10^{-12}
	500	24.960	9.20×10^{-13}	2.30×10^{-12}	9.84×10^{-12}

TABLE 4.4. *Example 3, case (c): CPU times vs. L^1-errors.*
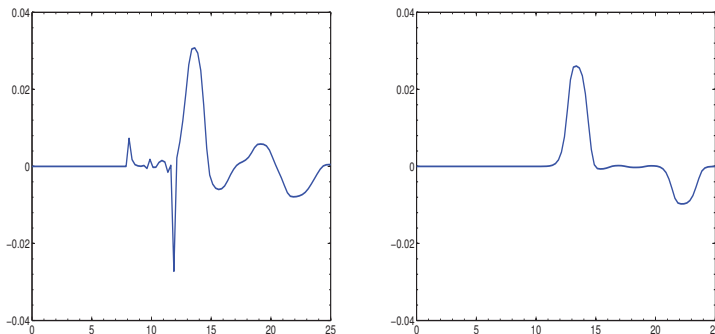
FIG. 4.5. *Example 4, case (a): the difference between h and the background moving steady state water depth for the Old (left) and New (right) Schemes. 100 uniform cells and $\eta = 0.05$ are used.*

moving steady state water depth. As one can see, the Old Scheme generates large spurious oscillations in the area over the bottom bump. As we refine the mesh to 1000 uniform cells, the magnitude of the oscillations decreases (see figures 4.8–4.10) since, as expected, it is proportional to the size of the truncation error. On the other hand, the
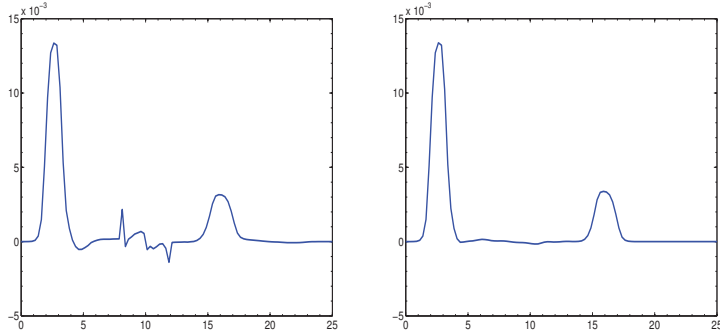
FIG. 4.6. *Example 4, case (b): the difference between h and the background moving steady state water depth for the Old (left) and New (right) Schemes. 100 uniform cells and $\eta = 0.05$ are used.*
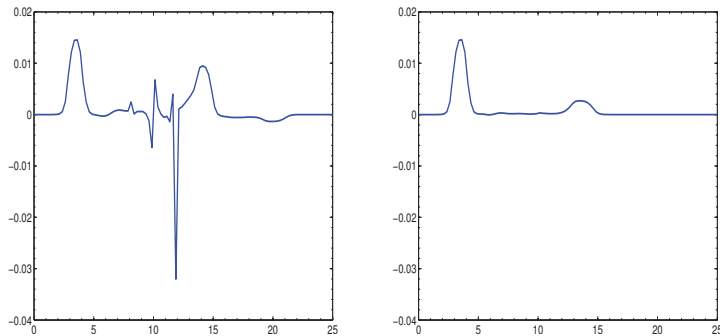

FIG. 4.7. *Example 4, case (c): the difference between h and the background moving steady state water depth for the Old (left) and New (right) Schemes. 100 uniform cells and $\eta = 0.05$ are used.*
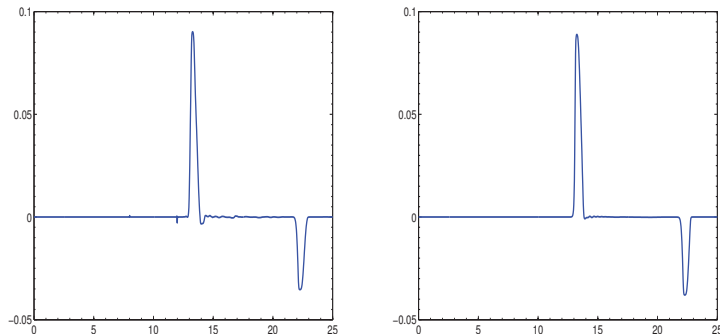
FIG. 4.8. *Example 4, case (a): Same as in Figure 4.5, but using 1000 uniform cells.*

results obtained by the New Scheme are oscillation-free on both coarse and fine meshes.

Finally, we take a smaller perturbation with $\eta = 0.001$ and perform the same comparison test. The results reported in figures 4.11–4.16 clearly demonstrate that in the case of smaller perturbation, the New Scheme is still oscillation-free while the oscillations generated by the Old Scheme are large even when a fined mesh of 1000 uniform
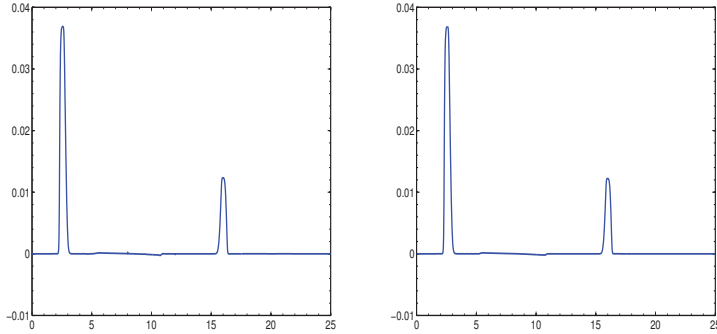
FIG. 4.9. *Example 4, case (b): Same as in Figure 4.6, but using 1000 uniform cells.*
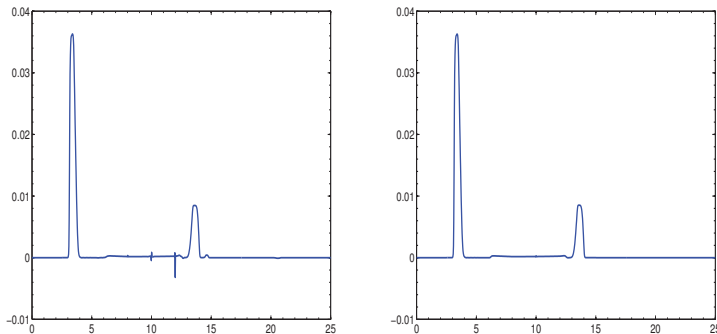
FIG. 4.10. *Example 4, case (c): Same as in Figure 4.7, but using 1000 uniform cells.*

cell is used.
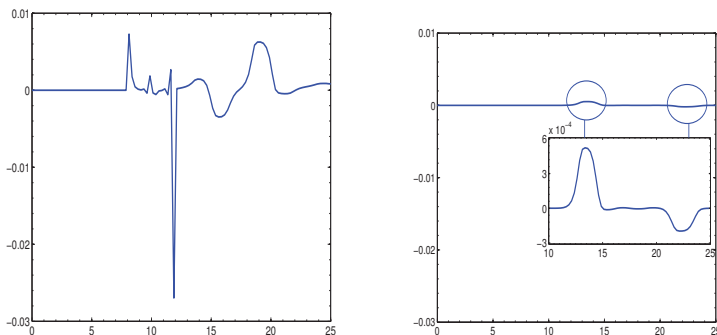
FIG. 4.11. *Example 4, case (a): the difference between h and the background moving steady state water depth for the Old (left) and New (right) Schemes. 100 uniform cells and $\eta = 0.001$ are used.*

Example 5 — convergence to steady states (discontinuous bottom topography). In this example, we study the convergence in time towards steady flow over a bump with the discontinuous bottom topography function (4.2). Here, we only show the results for the transcritical flow without a shock (we take the same initial and
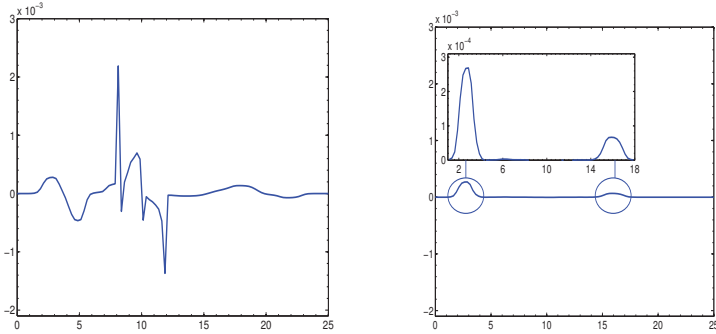
FIG. 4.12. *Example 4, case (b): the difference between h and the background moving steady state water depth for the Old (left) and New (right) Schemes. 100 uniform cells and $\eta = 0.001$ are used.*
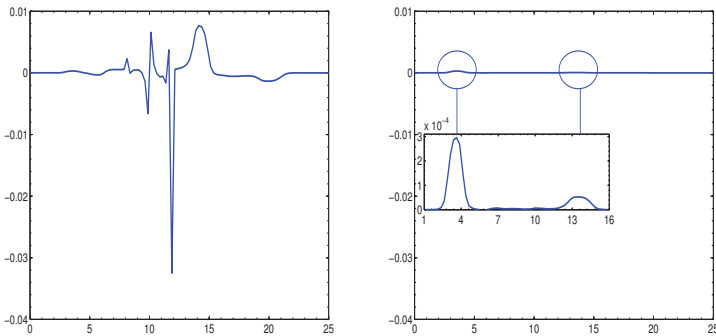
FIG. 4.13. *Example 4, case (c): the difference between h and the background moving steady state water depth for the Old (left) and New (right) Schemes. 100 uniform cells and $\eta = 0.001$ are used.*
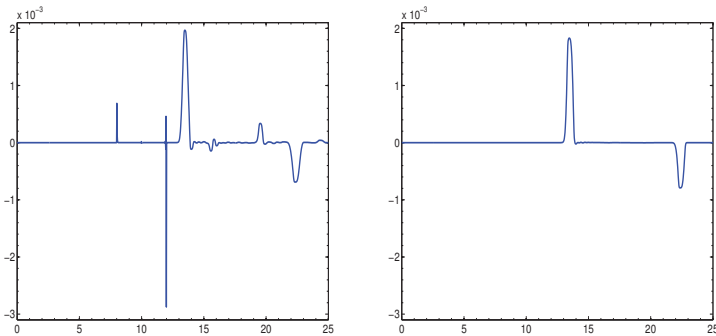
FIG. 4.14. *Example 4, case (a): Same as in Figure 4.11, but using 1000 uniform cells.*

boundary conditions as in Example 3, case (c)). In Figure 4.17, we compare the numerical solutions obtained by the New and Old Schemes at $t = 200$ using 200 uniform cells. The corresponding CPU times vs. the L^1-norm of the h-, q-, and E-errors are reported in Table 4.5. As one can clearly see, the New Scheme outperforms the Old Scheme in the case of discontinuous bottom topography though, as expected, the magnitude of the
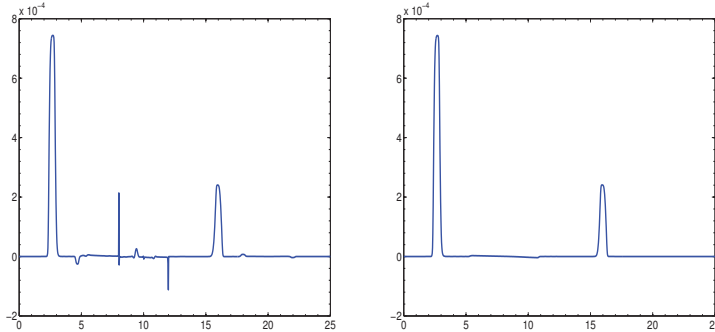
FIG. 4.15. *Example 4, case (b): Same as in Figure 4.12, but using 1000 uniform cells.*
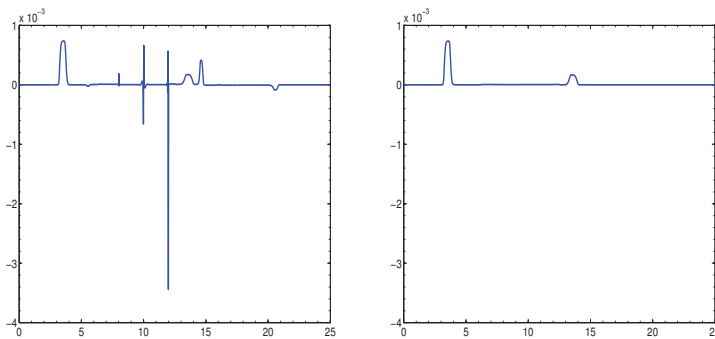

FIG. 4.16. *Example 4, case (c): Same as in Figure 4.13, but using 1000 uniform cells.*
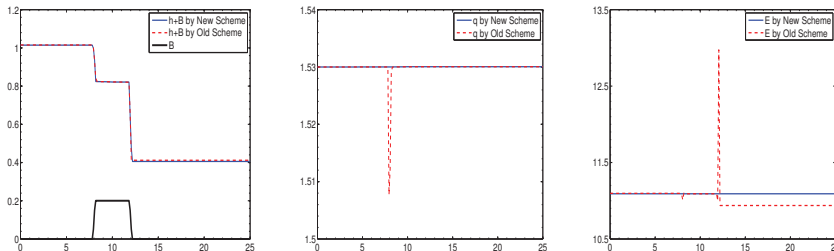

FIG. 4.17. *Example 5: $h+B$ (left), q (middle), and E (right) computed by the New and Old Schemes.*

errors is now larger than in the case of smooth B.

REMARK 4.3. We have also performed the numerical experiments using the discontinuous bottom topography function (4.2) and the initial-boundary data corresponding to cases (a) and (b) in Example 3. Our numerical experiments (not reported here for the sake of brevity) demonstrate that in these two cases, the accuracy of the New Scheme is practically not affected by the presence of the discontinuity in B, while the accuracy of the Old Scheme substantially deteriorates.

Example 6 — small perturbations of moving-water equilibria (discontinuous bottom topography). In this example, we test the ability of the New and

Scheme	Final time	CPU time	h-error	q-error	E-error
Old	200	3.3228	1.08×10^{-1}	5.88×10^{-3}	2.2747
	300	5.3040	1.05×10^{-1}	5.40×10^{-3}	2.2734
	400	6.9108	1.03×10^{-1}	5.26×10^{-3}	2.2729
	500	8.4397	1.03×10^{-1}	5.20×10^{-3}	2.2726
New	200	10.452	7.78×10^{-3}	7.54×10^{-4}	6.16×10^{-3}
	300	16.115	4.74×10^{-3}	3.09×10^{-4}	2.21×10^{-3}
	400	21.294	4.36×10^{-3}	1.12×10^{-6}	1.18×10^{-4}
	500	26.895	4.36×10^{-3}	1.06×10^{-6}	1.18×10^{-4}

TABLE 4.5. *Example 5: CPU times vs. L^1-errors.*
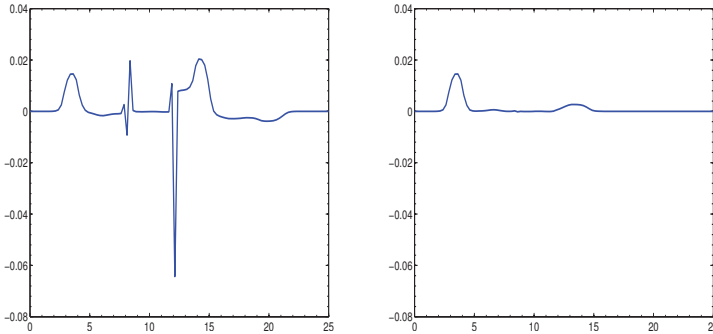
FIG. 4.18. *Example 6: the difference between h and the background moving steady state water depth for the Old (left) and New (right) Schemes. 100 uniform cells and $\eta = 0.05$ are used.*
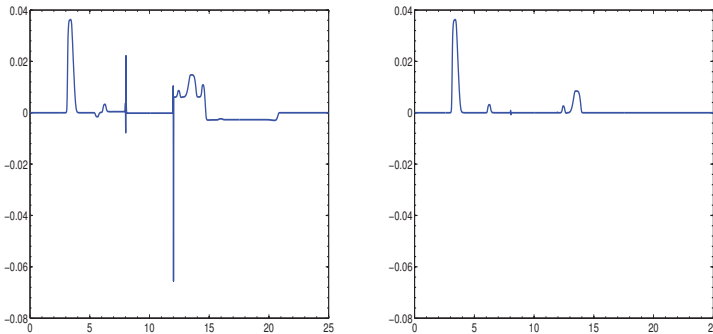

FIG. 4.19. *Example 6: Same as in Figure 4.18, but using 1000 uniform cells.*

Old Schemes to capture small perturbations of the moving-water equilibria studied in Example 2 with the discontinuous bottom topography function (4.2). We add the same positive numbers as in Example 4 (either $\eta = 0.05$ or $\eta = 0.001$) to the initial water depth in the region $x \in [5.75, 6.25]$ to generate small perturbations of the moving-water steady states. As in Example 5, we only show the results for the transcritical flow without a shock. We compute the solutions until the final time $t = 1.5$ using either 100 or 1000
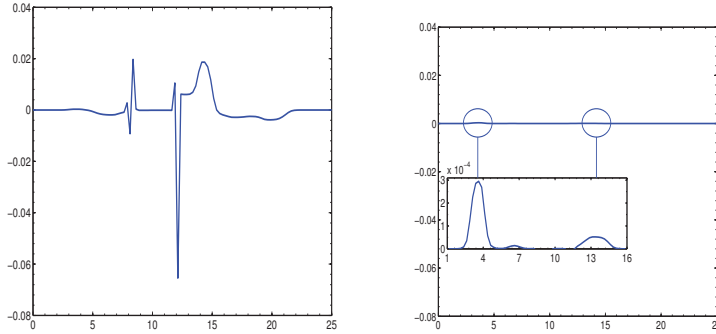
FIG. 4.20. *Example 6: the difference between h and the background moving steady state water depth for the Old (left) and New (right) Schemes. 100 uniform cells and $\eta = 0.001$ are used.*
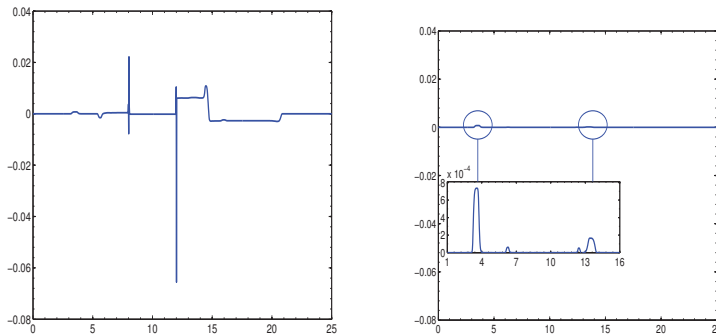

FIG. 4.21. *Example 6: Same as in Figure 4.20, but using 1000 uniform cells.*
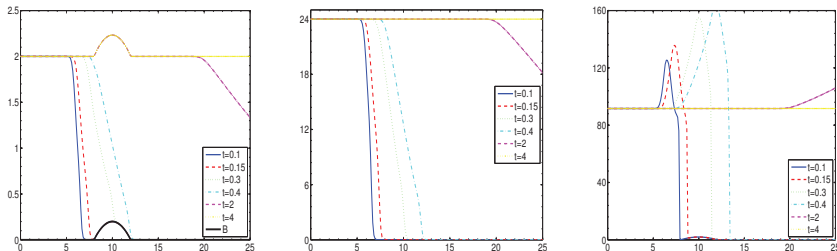

FIG. 4.22. *Example 7: $h + B$ (left), q (middle), and E (right) computed by the New Scheme.*

uniform cells. The obtained results, reported in figures 4.18–4.21, clearly demonstrate that in the case of discontinuous B, the New Scheme still captures small perturbations of the moving-water steady state much more accurately than the Old Scheme.

Example 7 — Riemann problem. In this example, we test positivity preserving property of the New Scheme. We modify the initial data of Example 3, case (a):

$$h(x,0) = \begin{cases} 2, \text{ if } x < 5, \\ 0, \text{ otherwise,} \end{cases} \qquad q(x,0) = \begin{cases} 24, \text{ if } x < 5, \\ 0, \text{ otherwise,} \end{cases}$$

and take the same boundary conditions as in Example 3, case (a). We compute the solutions using 200 uniform cells. Figure 4.22 shows the results at times $t = 0.1, 0.15, 0.3, 0.4, 2, 4$. As one can clearly see, the water flow runs through the bump smoothly and by $t = 4$ it reaches the same steady state as in Example 3, case (a) as expected.

REFERENCES

[1] E. Audusse, F. Bouchut, M.-O. Bristeau, R. Klein, and B. Perthame, *A fast and stable well-balanced scheme with hydrostatic reconstruction for shallow water flows*, SIAM J. Sci. Comput., 25, 2050–2065, 2004.

[2] A. Bollermann, G. Chen, A. Kurganov, and S. Noelle, *A well-balanced reconstruction for wet/dry fronts for the shallow water equations*, J. Sci. Comput., 56, 267–290, 2013.

[3] A. Bollermann, S. Noelle, and M. Lukáčová-Medvid'ová, *Finite volume evolution Galerkin methods for the shallow water equations with dry beds*, Commun. Comput. Phys., 10, 371–404, 2011.

[4] F. Bouchut and T. Morales, *A subsonic-well-balanced reconstruction scheme for shallow water flows*, SIAM J. Numer. Anal., 48, 1733–1758, 2010.

[5] S. Bryson, Y. Epshteyn, A. Kurganov, and G. Petrova, *Well-balanced positivity preserving central-upwind scheme on triangular grids for the Saint-Venant system*, M2AN Math. Model. Numer. Anal., 45, 423–446, 2011.

[6] M.J. Castro, J.A. López-García, and C. Parés, *High order exactly well-balanced numerical methods for shallow water systems*, J. Comput. Phys., 246, 242–264, 2013.

[7] J. Gallardo, C. Parés, and M. Castro, *On a well-balanced high-order finite volume scheme for shallow water equations with topography and dry areas*, J. Comput. Phys., 227, 574–601, 2007.

[8] L. Gosse, *A well-balanced flux-vector splitting scheme designed for hyperbolic systems of conservation laws with source terms*, Comput. Math. Appl., 39, 135–159, 2000.

[9] S. Gottlieb, D. Ketcheson, and C.-W. Shu, *Strong stability preserving Runge–Kutta and multistep time discretizations*, World Scientific Publishing Co. Pte. Ltd., Hackensack, NJ, 2011.

[10] S. Gottlieb, C.-W. Shu, and E. Tadmor, *Strong stability-preserving high-order time discretization methods*, SIAM Rev., 43, 89–112, 2001.

[11] N. Goutal and F. Maurel, *Proceedings of the second workshop on dam-break wave simulation*, tech. report, Technical Report HE-43/97/016/A, Electricité de France, Département Laboratoire National d'Hydraulique, Groupe Hydraulique Fluviale, 1997.

[12] S. Jin and X. Wen, *Two interface-type numerical methods for computing hyperbolic systems with geometrical source terms having concentrations*, SIAM J. Sci. Comput., 26, 2079–2101, 2005.

[13] A. Khan and W. Lai, *Modeling Shallow Water Flows Using the Discontinuous Galerkin Method*, CRC Press, Boca Raton, FL, 2014.

[14] A. Kurganov and D. Levy, *Central-upwind schemes for the Saint-Venant system*, M2AN Math. Model. Numer. Anal., 36, 397–425, 2002.

[15] A. Kurganov and C.-T. Lin, *On the reduction of numerical dissipation in central-upwind schemes*, Commun. Comput. Phys., 2, 141–163, 2007.

[16] A. Kurganov, S. Noelle, and G. Petrova, *Semi-discrete central-upwind scheme for hyperbolic conservation laws and Hamilton–Jacobi equations*, SIAM J. Sci. Comput., 23, 707–740, 2001.

[17] A. Kurganov and G. Petrova, *A second-order well-balanced positivity preserving central-upwind scheme for the Saint-Venant system*, Commun. Math. Sci., 5, 133–160, 2007.

[18] A. Kurganov and G. Petrova, *A central-upwind scheme for nonlinear water waves generated by submarine landslides*, in Hyperbolic problems: theory, numerics, applications (Lyon 2006), S. Benzoni-Gavage and D. Serre (eds.), Springer, 635–642, 2008.

[19] A. Kurganov and E. Tadmor, *New high resolution central schemes for nonlinear conservation laws and convection-diffusion equations*, J. Comput. Phys., 160, 241–282, 2000.

[20] R. LeVeque, *Balancing source terms and flux gradients in high-resolution Godunov methods: the quasi-steady wave-propagation algorithm*, J. Comput. Phys., 146, 346–365, 1998.

[21] K.-A. Lie and S. Noelle, *On the artificial compression method for second-order nonoscillatory central difference schemes for systems of conservation laws*, SIAM J. Sci. Comput., 24, 1157–1174, 2003.

[22] H. Nessyahu and E. Tadmor, *Nonoscillatory central differencing for hyperbolic conservation laws*, J. Comput. Phys., 87, 408–463, 1990.

[23] S. Noelle, Y. Xing, and C.-W. Shu, *High-order well-balanced finite volume WENO schemes for shallow water equation with moving water*, J. Comput. Phys., 226, 29–58, 2007.

[24] B. Perthame and C. Simeoni, *A kinetic scheme for the Saint-Venant system with a source term*, Calcolo, 38, 201–231, 2001.

[25] M. Ricchiuto and A. Bollermann, *Stabilized residual distribution for shallow water simulations*, J. Comput. Phys., 228, 1071–1115, 2009.

[26] G. Russo, *Central schemes for conservation laws with application to shallow water equations*, in Trends and Applications of Mathematics to Mechanics, Springer Milan, 225–246, 2005.

[27] G. Russo and A. Khe, *High order well balanced schemes for systems of balance laws*, in Hyperbolic problems: theory, numerics and applications, Proc. Sympos. Appl. Math., Amer. Math. Soc., Providence, RI, 67, 919–928, 2009.

[28] C.-W. Shu, *Total-variation-diminishing time discretizations*, SIAM J. Sci. Comput., 6, 1073–1084, 1988.

[29] C.-W. Shu and S. Osher, *Efficient implementation of essentially non-oscillatory shock-capturing schemes*, J. Comput. Phys., 77, 439–471, 1988.

[30] P. Sweby, *High resolution schemes using flux limiters for hyperbolic conservation laws*, SIAM J. Numer. Anal., 21, 995–1011, 1984.

[31] B. van Leer, *Towards the ultimate conservative difference scheme. V. A second-order sequel to Godunov's method*, J. Comput. Phys., 32, 101–136, 1979.

[32] M. Vazquez-Cendon, *Improved treatment of source terms in upwind schemes for the shallow water equations in channels with irregular geometry*, J. Comput. Phys., 148, 497–526, 1999.

[33] Y. Xing, *Exactly well-balanced discontinuous Galerkin methods for the shallow water equations with moving water equilibrium*, J. Comput. Phys., 257, 536–553, 2014.

[34] Y. Xing and C.-W. Shu, *A survey of high order schemes for the shallow water equations*, J. Math. Study, 47, 221–249, 2014.

[35] Y. Xing, C.-W. Shu, and S. Noelle, *On the advantage of well-balanced schemes for moving-water equilibria of the shallow water equations*, J. Sci. Comput., 48, 339–349, 2011.